Terahertz Near-Field Vectorial Imaging of Subwavelength Apertures and Aperture Arrays

J. R. Knab[1*], A. J. L. Adam[1], M. Nagel[2], E. Shaner[3], M. A. Seo[4], D. S. Kim[4] and P. C. M. Planken[1]

[1]*Delft University of Technology, Faculty of Applied Sciences, Department of Imaging Science and Technology, Optics Research Group*
Lorentzweg 1, 2628 CJ Delft, The Netherlands

[2]*Institut für Halbleitertechnik, RWTH Aachen University,*
Sommerfeldstr. 24 52074 Aachen, Germany

[3]*Sandia National Laboratories*
Albuquerque, New Mexico 87185 USA

[4]*Center for Subwavelength Optics and Department of Physics and Astronomy, Seoul National University*
Seoul 151-747, Korea

[*]*Corresponding author: J.R.Knab@tudelft.nl*

Abstract: We present measurements of the complete terahertz (THz) electric near-field distribution, E_x, E_y and E_z, in both the time- and frequency-domains, for subwavelength apertures and subsections of subwavelength aperture arrays. Measuring the individual components of the THz near-field with subwavelength spatial resolution, as they emerge from these structures, illustrates how the field interacts with the apertures. We observe the small but measurable y- and z-components of the electric field for both single apertures and arrays. Resonant contributions, attributed to Bloch modes, are detected and we observe the presence of a longitudinal field component, E_z, within the different array apertures, which can be attributed to a diffractive effect. These measurements illustrate in detail the individual THz field components emerging from subwavelength apertures and provide a direct measure of two important mechanisms that contribute to the net transmission of light through arrays.

OCIS codes: (110.6795) Terahertz Imaging; (050.6624) Subwavelength structures; (050.1220) Apertures.

References and links

1. T. W. Ebbesen, H. J. Lezec, H. F. Ghaemi, T. Thio, and P. A. Wolff, "Extraordinary optical transmission through sub-wavelength hole arrays," Nature (London) **391,** 667–669 (1998).
2. A. Degiron and T. W. Ebbesen, "The role of localized surface plasmon modes in the enhanced transmission of periodic subwavelength apertures," J. Opt. A. Pure Appl. Opt. **7,** S90–S96 (2005).
3. H. F. Ghaemi, T. Thio, D. E. Grupp, T. W. Ebbesen, and H. J. Lezec, "Surface plasmons enhance optical transmission through subwavelength holes," Phys. Rev. B **58,** 6779–6782 (1998).
4. A. Krishnan, T. Thio, T. J. Kim, H. J. Lezec, T. W. Ebbesen, P. A. Wolff, J. Pendry, L. Martin-Moreno, and F. J. Garcia-Vidal, "Evanescently coupled resonance in surface plasmon enhanced transmission," Opt. Commun. **200,** 1–7 (2001).

#113121 - $15.00 USD Received 19 Jun 2009; revised 7 Aug 2009; accepted 7 Aug 2009; published 11 Aug 2009

5. Z. Ruan and M. Qiu, "Enhanced Transmission through Periodic Arrays of Subwavelength Holes: The Role of Localized Waveguide Resonances," Phys. Rev. Lett. **96,** 233901 (2006).
6. J. Masson, A. Podzorov, and G. Gallot, "Anomalies in the disappearance of the extraordinary electromagnetic transmission in subwavelength hole arrays," Opt. Express **16,** 4719–4730 (2008).
7. K. J. Klein Koerkamp, S. Enoch, F. B. Segerink, N. F. van Hulst, and L. Kuipers, "Strong Influence of Hole Shape on Extraordinary Transmission through Periodic Arrays of Subwavelength Holes," Phys. Rev. Lett. **92,** 183901 (2004).
8. C. Genet and T. W. Ebbesen, "Light in tiny holes," Nature (London) **445,** 39–46 (2007).
9. R. Gordon, D. Sinton, K. L. Kavanagh, and A. G. Brolo, "A New Generation of Sensors Based on Extraordinary Optical Transmission," Acct. Chem. Res. **41,** 1049–1057 (2008).
10. T. Ribaudo, E. A. Shaner, S. S. Howard, C. Gmachl, X. J. Wang, F.-S. Choa, and D. Wasserman, "Active control and spatial mapping of mid-infrared propagating surface plasmons," Opt. Express **17,** 7019–7024 (2009).
11. C.-C. Chen, "Transmission of Microwave Through Perforated Flat Plates of Finite Thickness," IEEE Trans. Microwave Theory Tech. **MTT-21,** 1–6 (1973).
12. R. Ulrich and M. Tacke, "Submillimeter waveguiding on periodic metal structure," Appl. Phys. Lett. **22,** 251–253 (1973).
13. A. Mitsuishi, Y. Otsuka, S. Fujita, and H. Yoshinaga, "Metal Mesh Filters in the Far Infrared Region," Japanese J. Appl. Phys. **2,** 574–577 (1963).
14. C.-C. Chen, "Transmission Through a Conducting Screen Perforated Periodically with Apertures," IEEE Trans. Microwave Theory Tech. **MTT-18,** 627–632 (1970).
15. J. Gómez Rivas, C. Schotsch, P. Haring Bolivar, and H. Kurz, "Enhanced transmission of THz radiation through subwavelength holes," Phys. Rev. B **68,** 201306 (2003).
16. D. Qu, D. Grischkowsky, and W. Zhang, "Terahertz transmission properties of thin, subwavelength metallic hole arrays," Opt. Lett. **29,** 896–898 (2004).
17. H. Cao and A. Nahata, "Resonantly enhanced transmission of terahertz radiation through a periodic array of subwavelength apertures," Opt. Express **12,** 1004–1010 (2004).
18. E. Hendry, F. J. Garcia-Vidal, L. Martin-Moreno, J. Gómez Rivas, M. Bonn, A. P. Hibbins, and M. J. Lockyear, "Optical Control over Surface-Plasmon-Polariton-Assisted THz Transmission through a Slit Aperture," Phys. Rev. Lett. **100,** 123901 (2008).
19. A. K. Azad, Y. Zhao, W. Zhang, and M. He, "Effect of dielectric properties of metals on terahertz transmission in subwavelength hole arrays," Opt. Lett. **31,** 2637–2639 (2006).
20. D. Qu and D. Grischkowsky, "Observation of a New Type of THz Resonance of Surface Plasmons Propagating on Metal-Film Hole Arrays," Phys. Rev. Lett. **93,** 196804 (2004).
21. H. Cao and A. Nahata, "Influence of aperture shape on the transmission properties of a periodic array of subwavelength apertures," Opt. Express **12,** 3664–3672 (2004).
22. S. Ducourtieux, S. Grésillon, J. C. Rivoal, C. Vannier, C. Bainier, D. Courjon, and H. Cory, "Imaging subwavelength holes in chromium films in scanning near-field optical microscopy. Comparison between experiments and calculation," Eur. Phys. J. Appl. Phys. **26,** 35–43 (2004).
23. M. A. Seo, A. J. L. Adam, J. H. Kang, J. W. Lee, K. J. Ahn, Q. H. Park, P. C. M. Planken, and D. S. Kim, "Near field imaging of terahertz focusing onto rectangular apertures," Opt. Express **16,** 20484–20489 (2008).
24. O. Mitrofanov, M. Lee, J. W. P. Hsu, L. N. Pfeiffer, K. W. West, J. D. Wynn, and J. F. Federici, "Terahertz pulse propagation through small apertures," Appl. Phys. Lett. **79,** 907–909 (2001).
25. A. Bitzer and M. Walther, "Terahertz near-field imaging of metallic subwavelength holes and hole arrays," Appl. Phys. Lett. **92,** 231101 (2008).
26. A. Bitzer, H. Merbold, A. Thoman, T. Feurer, H. Helm, and M. Walther, "Terahertz near-field imaging of electric and magnetic resonances of a planar metamaterial," Opt. Express **17,** 3826–3834 (2009).
27. A. J. L. Adam, J. M. Brok, M. A. Seo, K. J. Ahn, D. S. Kim, J. H. Kang, Q. H. Park, M. Nagel, and P. C. M. Planken, "Advanced terahertz electric near-field measurements at sub-wavelength diameter metallic apertures," Opt. Express **16,** 7407–7417 (2008).
28. M. Mrejen, A. Israel, H. Taha, M. Palchan, and A. Lewis, "Near-field characterization of extraordinary optical transmission in sub-wavelength aperture arrays," Opt. Express **15,** 9129–9138 (2007).
29. H. Gao, J. Henzie, and T. W. Odom, "Direct Evidence for Surface Plasmon-Mediated Enhanced Light Transmission through Metallic Nanohole Arrays," Nano Lett. **6,** 2104–2108 (2006).
30. S. C. Hohng, Y. C. Yoon, D. S. Kim, V. Malyarchuk, R. Müller, Ch. Lienau, J. W. Park, K. H. Yoo, J. Kim, H. Y. Ryu, and Q. H. Park, "Light emission from the shadows: Surface plasmon nano-optics at near and far fields," Appl. Phys. Lett. **81,** 3239–3241 (2002).
31. G. Zhao, R. N. Schouten, N. C. J. van der Valk, W. Th. Wenckebach, and P. C. M. Planken, "Design and performance of a THz emission and detection setup based on a semi-insulating GaAs emitter," Rev. Sci. Instrum. **73,** 1715–1719 (2002).
32. R. Chakkittakandy, J. A. Corver, and P. C. M. Planken, "Quasi-near field terahertz generation and detection," Opt. Express **16,** 12794–12805 (2008).
33. N. C. J. van der Valk, T. Wenckebach, and P. C. M. Planken, "Full mathematical description of electro-optic

#113121 - $15.00 USD Received 19 Jun 2009; revised 7 Aug 2009; accepted 7 Aug 2009; published 11 Aug 2009

detection in optically isotropic crystals," J. Opt. Soc. Am. B **21,** 622–631 (2004).
34. M. A. Seo, A. J. L. Adam, J. H. Kang, J. W. Lee, S. C. Jeoung, Q. H. Park, P. C. M. Planken, and D. S. Kim, "Fourier-transform terahertz near-field imaging of one-dimensional slit arrays: mapping of electric-field-, magnetic-field-, and Poynting vectors," Opt. Express **15,** 11781–11789 (2007).
35. C. J. Bouwkamp, "On Bethe's Theory Of Diffraction By Small Holes," Philips Res. Rep. **5,** 321–332 (1950).
36. J. Bravo-Abad, L. Martín-Moreno, F. J. García-Vidal, E. Hendry, and J. Gómez Rivas, "Transmission of light through periodic arrays of square holes: From a metallic wire mesh to an array of tiny holes," Phys. Rev. B **76,** 241102 (2007).
37. R. W. Wood, "Anomalous Diffraction Gratings," Phys. Rev. **48,** 928–936 (1935).
38. T. J. Kim, T. Thio, T. W. Ebbesen, D. E. Grupp, and H. J. Lezec, "Control of optical transmission through metals perforated with subwavelength hole arrays," Opt. Lett. **24,** 256–258 (1999).
39. J. B. Pendry, L. Martín-Moreno, and F. J. Garcia-Vidal, "Mimicking Surface Plasmons with Structured Surfaces," Science **305,** 847–848 (2004).
40. F. J. García de Abajo, "Colloquium: Light scattering by particle and hole arrays," Rev. Mod. Phys. **79,** 1267–1290 (2007).
41. R. Gordon, "Bethe's aperture theory for arrays," Phys. Rev. A **76,** 053806 (2007).
42. H. Liu and P. Lalanne, "Microscopic theory of the extraordinary optical transmission," Nature (London) **452,** 728–731 (2008).

1. Introduction

Enhanced optical transmission (EOT) in subwavelength hole arrays, first reported by Ebbesen et al. [1], has been the subject of many studies in recent years. Several of these studies were aimed at elucidating and exploring the underlying physical mechanism of EOT [2–7], which has been attributed to surface plasmon (SP) resonances. A fundamental understanding of EOT has opened the door to several potentially interesting applications, including but not limited to biological and chemical sensing ([8, 9] and references therein), active, directional control of SP propagation [10] and optical filtering [8]. At microwave and far-infrared frequencies, electromagnetic properties of metallic meshes and hole arrays were investigated as far back as the 1960s and 70s [11–14]. However, as far as we can tell, experimental evidence for enhanced transmission at terahertz (THz) frequencies through periodic, subwavelength hole arrays was not reported until relatively recently, in the work of Rivas et al. [15], where the arrays were made in doped silicon wafers. The transmission enhancement was attributed to coupling of the incident light to surface plasmon polaritons. Subsequently, many studies emerged, investigating enhanced THz transmission in subwavelength hole arrays and other structures [16–21]. Most investigations of enhanced THz transmission have been conducted in the far field. However, in order to understand how light emerges from arrays, *near-field* measurements are vital [22–27], as shown in recent near-infrared- and visible-wavelength, near-field array measurements [28–30]. This is because near-field information, such as the presence and interaction of evanescent fields, surface waves and the spatial distribution of the surface charge density, is inevitably lost in the far field.

Recently, we reported on the measurement of the THz electric near-field behind a subwavelength-sized hole, which was directly integrated onto an electro-optic detection crystal [27]. The component of the electric field polarized perpendicular to the metal (E_z) was measured, and it was shown how light emerges from a subwavelength hole with unprecedented detail. In a related work, Bitzer et al. [25] reported measurements of the transverse electric field component, parallel to the incident field, behind subwavelength holes and finite-sized hole arrays in free-standing foils. In that work, the authors utilized a small dipole antenna to measure the THz field and required a minimum distance of $\sim 35\,\mu$m between the samples and detector. This distance is expected to yield smaller near-field amplitudes and significant loss of detail, relative to the direct sample-detector integration utilized in the work of Adam et al. [27] and in this work.

Here we report on the measurement of *all three* electric near-field components, $E_x(t)$, $E_y(t)$

#113121 - $15.00 USD Received 19 Jun 2009; revised 7 Aug 2009; accepted 7 Aug 2009; published 11 Aug 2009

and $E_z(t)$, behind single subwavelength-sized holes and hole arrays with different periodicities. Our results reveal the presence of a significant y-component in the near field, measured directly behind the hole and hole arrays. Even for a single square hole, for which the y-component is expected to be small, a y-component is observed nonetheless, with deep sub-wavelength spatial resolution. In the hole arrays, we measure a significant longitudinal component of the electric field, E_z, *directly behind* the apertures and near the onset of diffraction, $\lambda = p\sqrt{\varepsilon}$, where p is the array period and ε is the dielectric constant of the substrate. This behavior is in strong contrast to the field distribution of a singular aperture and a cylindrical waveguide. We measure spectral signatures of surface plasmons in the arrays, for all field components, consistent with the theoretical predictions of Bloch modes. Our results provide insight into the near-field behavior of subwavelength structures, where various diffractive and resonant contributions combine to form the field transmission that is observed in the far field.

2. Experimental technique

THz time-domain spectroscopy (THz-TDS), with current transient THz generation and electro-optic detection [31], is used to image and characterize subwavelength structures in the near field, in both the time- and frequency-domain. An illustration showing how the samples are imaged is given in Fig. 1(a). THz light is focused onto subwavelength

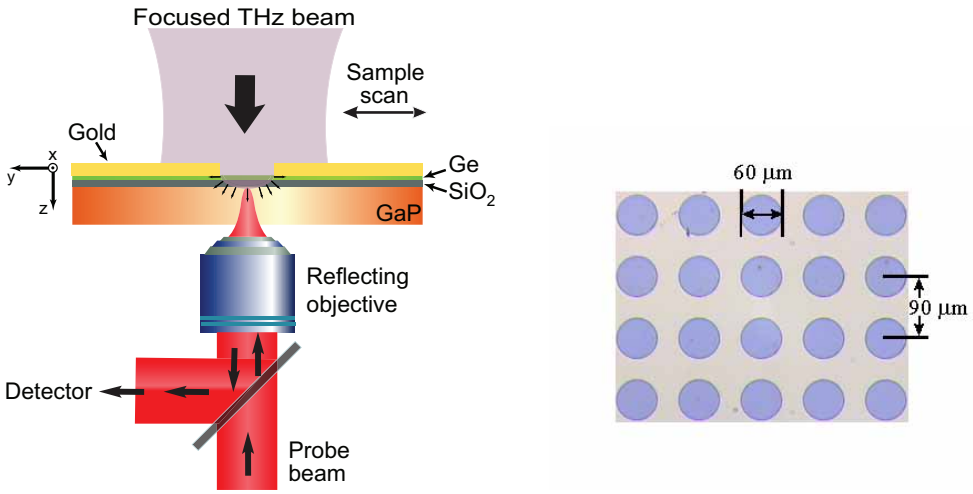

Fig. 1. (a) Near-field Imaging Setup (b) Microscope image of an array subsection with 90 μm periodicity.

structures using an off-axis parabolic mirror. The electric near-field is detected with an initially counter-propagating, near-infrared probe beam ($\lambda = 800$ nm) [23, 27, 32], which is tightly focused to a small spot immediately beneath the metal structure. The THz near-field elliptically polarizes the probe beam, which is reflected to a standard electro-optic detection setup. The delay between the probe beam and THz beam is modulated at 50 Hz, allowing us to measure a 25 ps-long THz transient in 10 ms. Samples are raster scanned in the focal plane of the THz beam, and the THz near-field is measured pixel by pixel, while the incident THz beam and the probe remain fixed. The x, y, and z-components of the THz electric near-field are measured by choosing a suitable probe beam polarization and crystal orientation for the electro-optic detection crystal. We use a (111) crystal orientation to measure the x- and y-components, and

#113121 - $15.00 USD Received 19 Jun 2009; revised 7 Aug 2009; accepted 7 Aug 2009; published 11 Aug 2009

a (100) crystal to measure the z-component [33, 34]. As we will show below, this setup has an estimated spatial resolution of $\sim 10\,\mu$m.

The advantage of using THz-TDS is that we directly measure the three electric near-field components in the time domain, giving us both the field amplitude and relative phase. This is an important distinction from measurements conducted at optical wavelengths, where typically only the optical power is measured [28–30]. Two subwavelength, circular aperture arrays with periods P = 90 μm and P = 160 μm, and identical aperture diameter (d = 60 μm), as well as a third, larger array (d = 200 μm; P = 300 μm) were studied in this work. A microscope image of the P = 90 μm array is shown in Fig. 1(b). The apertures are arranged in a square lattice and are formed in a 200 nm-thick gold layer that is deposited directly onto a GaP detection crystal, which has a thickness of $\sim 300\,\mu$m. The integration of the array directly on top of the detection crystal avoids complications arising from Fabry-Perot effects between the sample and detector. Single, isolated, circular apertures (d = 20 μm, 60 μm and 150 μm) as well as a square aperture with a side length of 200 μm, were also studied. The 150 μm, circular aperture and the square aperture are formed on the same wafers as the arrays; the 20 μm and 60 μm apertures are made in a 500 nm-thick gold layer, on a thicker GaP crystal ($\sim 500\,\mu$m). Note that the gold layer in all samples is thick enough to prevent significant direct transmission of THz radiation in the regions between apertures, since the skin depth of gold is ~80 nm at 1.0 THz.

3. Subwavelenth apertures

In Figs. 2(a)-(c), we plot amplitude images of the x-, y-, and z-components of the measured THz electric near-field at 0.2 THz for a single circular aperture, with a diameter of 150 μm. The scan

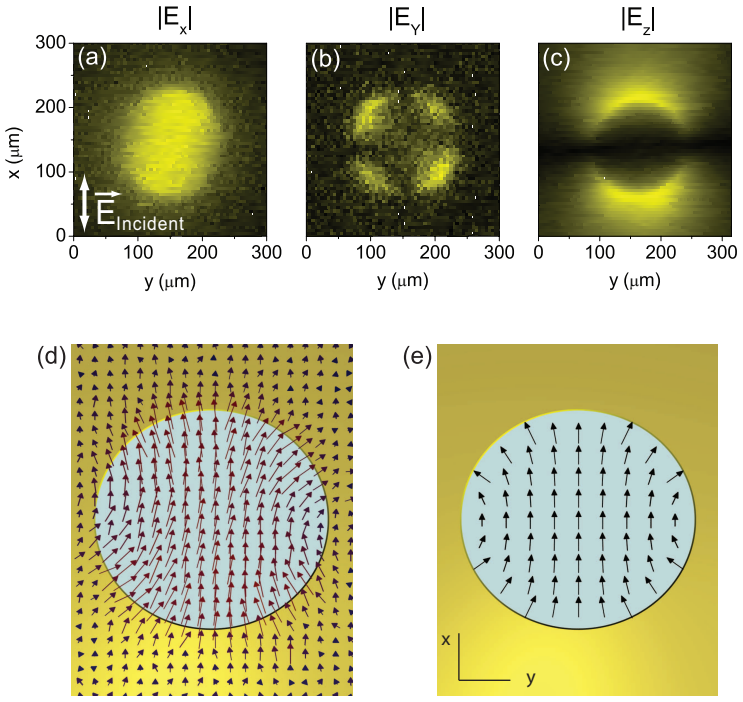

Fig. 2. THz electric near-field for a single, isolated, circular aperture (d = 150 μm) at 0.2 THz. Figures (a)-(c): $|E_x|$, $|E_y|$, and $|E_z|$. Scan area = 315 μm x 315 μm. Figure (d): Vector field plot illustrating measured transverse components of THz electric near-field. Figure (e): Vector field plot calculated from Bouwkamp's model.

#113121 - $15.00 USD Received 19 Jun 2009; revised 7 Aug 2009; accepted 7 Aug 2009; published 11 Aug 2009

area for these data was 315 μm x 315 μm. The bright areas correspond to high field amplitude and dark areas correspond to low field amplitude. The polarization of the incident THz beam is indicated in the figure. These data completely characterize the THz field in a plane immediately beneath the aperture. The free-space wavelength corresponding to a frequency of 0.2 THz is 1.5 mm, 10x larger than the aperture diameter. The figure shows that the x-component is strongest in the middle of the aperture and has a non-spherically symmetric spatial distribution. This shape follows from the incident field polarization which breaks the spherical symmetry, along with the requirement that at the metal surface, there can be no field component parallel to the metal. The y-component of the field consists of four lobes inside the aperture, with adjacent lobes 180° out of phase. The z-component of the field, which can be directly related to the surface charge density, is concentrated at the top and bottom aperture edges, where each lobe is also 180° out of phase, confirming earlier results [27].

These results can be understood by realizing that at THz frequencies, where metals act much like perfect conductors, the boundary conditions for the time-dependent electric field dictate that the field must always be perpendicular to the metal surface. Inside the hole, therefore, at the rim of the aperture, a y-component must be created. This is shown in Fig. 2(d), where we present a vector field plot of the measured in-plane electric field components, E_x and E_y. The figure clearly shows that the in-plane electric field is perpendicular to the metal edge. Loosely speaking, the shape of the hole forces changes in the electric field direction, to fulfill the boundary conditions of the EM-field. In Fig. 2(e), we show a calculation of the in-plane electric field in the plane z = 0, calculated using Bouwkamp's model [35]. As Bouwkamp's model is based on a hole in a perfectly conducting, infinitely thin plane, infinitely strong fields are predicted at the edges of the hole. In Fig. 2(e), these field vectors are drawn with a finite length, and the figure can therefore only be used to compare the direction of the calculated and measured field vectors, not their lengths. Keeping this limitation in mind, we observe that the measurements and calculation are in good agreement with each other. The measurements also show a finite field just beyond the aperture rim, at the metal, whereas the model predicts that the in-plane field should be zero at the metal surface. This can be explained by the fact that the measurement technique also measures fields a short distance away from the metal, where finite in-plane fields are allowed [27].

The in-plane component of the field perpendicular to the incident field polarization can be particularly difficult to measure for certain aperture shapes. For example, the y-component for a square aperture is expected to be weaker than that observed in a circular aperture of similar dimensions, simply due to the geometry of the aperture. Figure 3 shows a measurement of E_y for a single, isolated, square aperture in a 200 nm-thick gold film at 0.2 THz. The aperture dimensions are 200 μm per side and the total scan area for this measurement is 400 μm per side. Bright color corresponds to positive field amplitude and dark color corresponds to the contrary. The dashed line shows the outline of the aperture. In general, this field component is orders of magnitude weaker than the propagating field, and is strongest very close to the aperture edge. The measurement technique employed here is sensitive enough to measure these extremely weak fields, precisely because the fields are measured in a plane that is very close to the sample structure where the near-fields are strongest.

One can begin to see the limit of our spatial resolution in Fig. 4, where we plot E_z for three different aperture diameters: 150 μm, 60 μm and 20 μm. The images are scaled according to aperture size. The figure shows that for decreasing aperture size, the shape of the aperture becomes relatively less well resolved. The spatial resolution can be difficult to quantify, since the aperture edges, in a plane immediately beneath the metal, do not behave like step functions with regard to the light transmission. However, based on these images, we can conservatively estimate that our spatial resolution is $\sim$10 μm. This estimate is consistent with

#113121 - $15.00 USD Received 19 Jun 2009; revised 7 Aug 2009; accepted 7 Aug 2009; published 11 Aug 2009

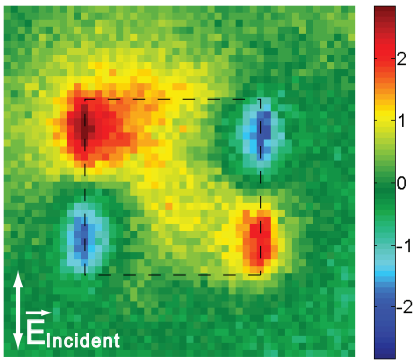

Fig. 3. $E_y(\omega t = 0)$ for a square aperture at 0.25 THz. Aperture dimensions: 200 μm x 200 μm. Scan Area: 400 μm x 400 μm. Bright color corresponds to positive field amplitude and dark color to negative field amplitude. The incident field polarization is indicated.

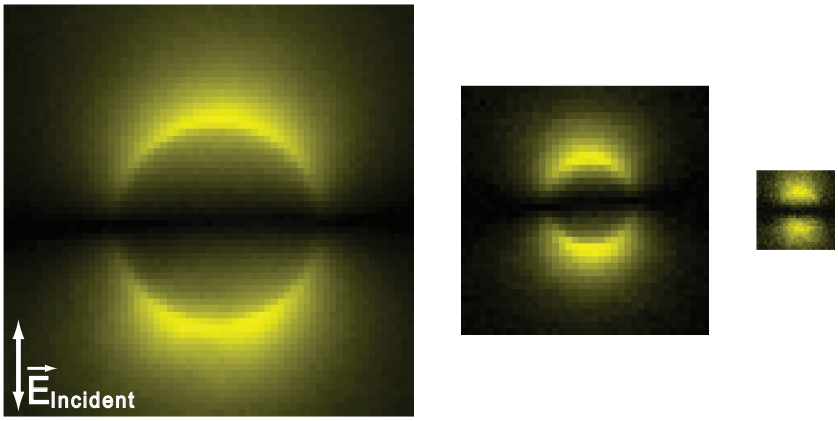

Fig. 4. Peak-peak amplitude images of E_z for circular apertures having three different diameters. From left to right: d = 150 μm, 60 μm and 20 μm; scan area = 315 μm x 315 μm, 190 μm x 190 μm, 60 μm x 60 μm, respectively.

our prior near-field measurements of a 100 μm-diameter hole, which showed sharp features in the z-component of the field measured at the edge of the hole [27]. Note that, although the three apertures in Fig. 4 resemble each other, the near-field spectra are not the same. The electric near-field measured underneath the smallest aperture contains mostly higher frequency components, as is expected for apertures of decreasing size.

4. Subwavelength circular aperture arrays

Near-field images of the THz peak-peak electric field amplitude for the P = 90 μm array are shown in Fig. 5. The scan dimensions are $\sim$200 μm x 200 μm. In Fig. 5(b) and (c), bright color corresponds to positive field amplitude and and dark color corresponds to negative field amplitude, while the color scale in Fig. 5(a) corresponds to positive field values only. These images correspond to a time when the emerging THz fields reach their maximum amplitude. Our measurements allow us to measure the sign of the individual field components. This can be seen in Figs. 5(b) and (c), where the blue and red colors correspond to field components that are

#113121 - $15.00 USD Received 19 Jun 2009; revised 7 Aug 2009; accepted 7 Aug 2009; published 11 Aug 2009

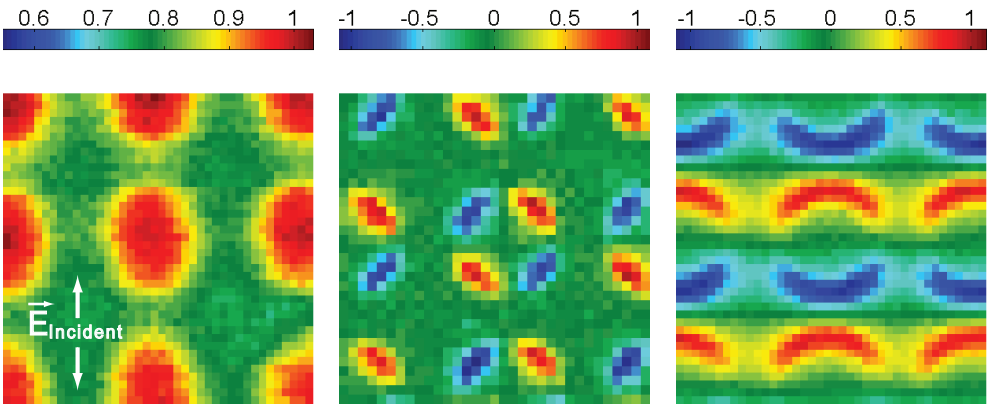

(a) E_x (b) E_y (c) E_z

Fig. 5. THz electric near-field for the P = 90 μm, subwavelength aperture array. Figures (a)-(c): time-domain, field amplitude images of an array subsection in the middle of the array. In each case, the images correspond to times when the THz field is maximum. Array dimesions: $\sim$ 1.4 mm per side. Scan dimensions: $\sim$200 μm x 200 μm. The incident THz field polarization is indicated on the left.

180° out of phase. We are capable of resolving images as well as obtaining spectral information down to $\sim$ 0.2 THz, which corresponds to a free-space wavelength that is 25x larger than the aperture diameter. This frequency is well below the waveguide cutoff frequency for a 60 μm diameter circular aperture, determined to be $\nu_c = 0.89$ THz. Here, ν_c is calculated assuming that the hole is filled with its dielectric substrate. This reduced cutoff is consistent with the observed behavior of single, isolated, subwavelength apertures reported in Adam et al. [27]. As in the case of the single aperture, these images, taken together, completely characterize the THz electric near-field in a plane immediately beneath the metal layer. Measuring the fields very close to the metal/dielectric interface again allows us to image the weaker, though non-negligible y- and z-components of the electric field.

THz-TDS allows us to obtain not only amplitude, but also relative phase information [25]. For instance, amplitude and phase images of E_z for the P = 90 μm array are shown in Fig. 6 at two different frequencies. The color bars correspond to the relative phase angle in degrees; red colors signify positive phase and blue colors signify negative phase. These frequency-domain data correspond to the same apertures shown in the peak amplitude, time-domain images in Fig. 5. The top two images in Fig. 6 show the amplitude and phase images at 0.468 THz. The amplitude image looks very similar to the peak amplitude image in Fig. 5. The phase image shows bands of positive and negative phase, indicating that the fields at the aperture edges are 180°out of phase. The amplitude and phase images, shown in Figs. 6(c) and (d) respectively, are plotted at a frequency of 1.0 THz. The relatively weaker, horizontal bands that appear between the apertures in Fig. 6(c) are consistent with the model proposed by Bravo-Abad et al. [36], in which the transmission is governed by interplay between resonant and nonresonant contributions, and the bands themselves represent a standing surface wave. Remarkably, at this frequency, the amplitude image shows concentration of field not only around the aperture edges, but also *within* the apertures. In fact, measurements of the field for a *single, isolated* aperture of identical size give no indication of similar features inside the hole. This is a strong indication that it somehow results from interactions between the holes. The fact that we do observe something might be caused by our measurement technique that likely integrates the THz field

#113121 - $15.00 USD Received 19 Jun 2009; revised 7 Aug 2009; accepted 7 Aug 2009; published 11 Aug 2009

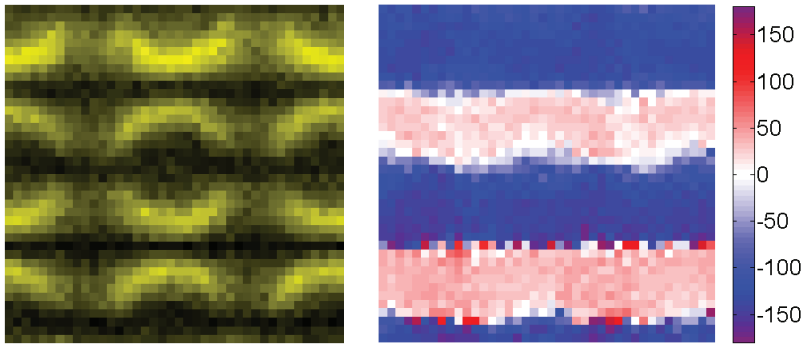

(a) $|E_z|$ at $\nu = 0.47$ THz (b) Φ_z at $\nu = 0.47$ THz

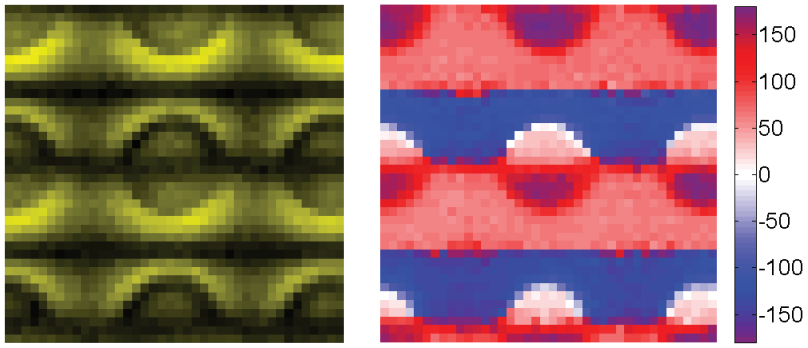

(c) $|E_z|$ at $\nu = 1.0$ THz (d) Φ_z at $\nu = 1.0$ THz

Fig. 6. Amplitude and phase images of P = 90 μm array for $\nu = 0.47$ THz and $\nu = 1.0$ THz. The color bar in each phase image corresponds to a range of angles from -180° to +180°.

over a small but finite distance in the electro-optic detection crystal [27]. To study the origin of the field we observe within the aperture, we plot in Fig. 7 the THz spectral transmission, normalized against the spectrum of the incident THz field, for a single isolated aperture (dotted line) and a single aperture in the center of an aperture array with 90 μm periodicity (solid line). The array transmission increases approximately linearly with frequency until it reaches a point at ~ 0.8 THz, where a peak begins to emerge. This peak reaches a maximum at 0.96 THz, very close to the waveguide cutoff ($\nu_c = 0.89$ THz) for a GaP-filled waveguide and also close to the frequency where we observe the emergence of a field *within* the aperture (see Fig. 6(c)). Nitrogen purging eliminates the possibility that these spectral features originate from water vapor absorption. The idea that this peak may originate from a waveguide resonance or otherwise 'deviant' waveguide behavior can be eliminated when one compares these data to the single aperture data. In that case, the normalized transmission increases linearly with frequency and appears to gradually level off near 1.0 THz. Note the absence of a comparably sharp peak near the cutoff frequency.

4.1. Diffractive contributions

In Fig. 8, we show time- and frequency-domain data for a single aperture in the middle of the P = 90 μm array. Samples are measured in a sealed, nitrogen purged environment, thus eliminating water vapor absorption and the possibility that the peak observed in the spectrum is an associated artifact. Figure 8(a) shows time-domain data for two pixels from the aperture

#113121 - $15.00 USD Received 19 Jun 2009; revised 7 Aug 2009; accepted 7 Aug 2009; published 11 Aug 2009

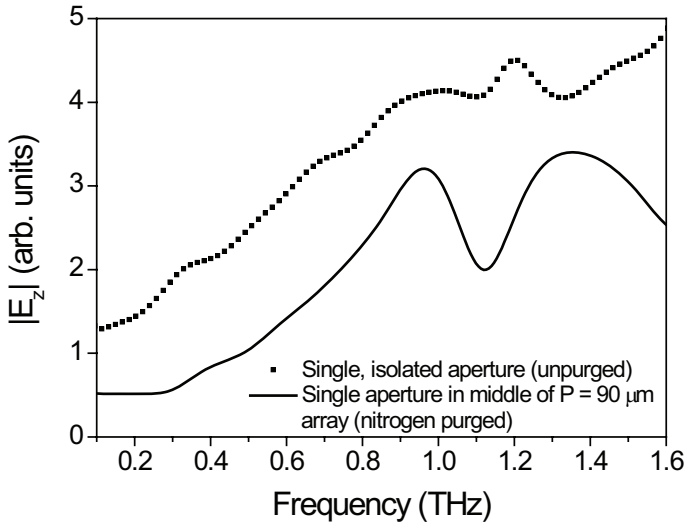

Fig. 7. Comparison of transmission for a single 60 μm-diameter aperture in the center of the P = 90 μm array (solid line) and for a single, isolated aperture having the same diameter (dotted line); both data sets correspond to a single pixel on the upper aperture edge and are normalized to the incident THz field. The single aperture was made in a 500 nm-thick gold layer that was deposited on a $\sim 500\,\mu m$ GaP crystal. The array data were recorded in a nitrogen-purged environment, while the single aperture data were not.

image. Three cases are plotted here: the raw uncut data from a single pixel on the aperture edge (dotted red line); the same data, windowed such that the first etalon pulse, which originates from multiple reflections within the GaP crystal, is excluded (solid red); and data from a single pixel in the middle of the aperture (solid blue), also windowed to exclude the first etalon pulse. The data for the time-domain amplitude image in Fig. 8 corresponds to a time of 3.81 ps, which is much earlier than the arrival of the first etalon pulse at $\sim$ 10 ps, thus eliminating the possibility that the field within the aperture is a Fabry-Perot effect. In Fig. 8(b), we show frequency-domain data for the two pixels corresponding to the time-dependent fields measured inside the aperture and at the aperture edge, as shown in Fig. 8(a). The field spectrum at the aperture edge exhibits a peak close to the waveguide cutoff, followed by a local minimum at $\sim$ 1.10 THz. We note that the positions of these spectral features can vary by a few tens of GHz in different pixels. This is likely due to a lower signal-to-noise ratio at this frequency. The peak we observe might be explained by increased diffractive contributions from the surrounding apertures that become more prominent as one approaches the cutoff frequency from above. In this picture, the combination of decreased transmission near the waveguide cutoff and increased diffraction at the longer wavelengths combine to produce a peak [27].

The field spectrum within the aperture is noteworthy. At low frequencies, the field within the aperture is very small. Evanescent light transmitted through the aperture is strongly diffracted and therefore, any longitudinal component we observe should be highly localized on the aperture edges. At $\sim$ 0.89 THz, the transmission begins to rapidly increase, reaching a peak at $\sim$ 1.10 THz. This peak is located at approximately the same frequency at which the first local minimum is observed in the spectrum from the aperture edge. The emergence of field within the array apertures is also observed in the time-domain; a movie showing the time-evolution of E_z as it emerges from the aperture shown in Fig. 8 is available online. If one considers how the collective arrangement of subwavelength apertures, in the form of a bigrating, interacts

#113121 - $15.00 USD Received 19 Jun 2009; revised 7 Aug 2009; accepted 7 Aug 2009; published 11 Aug 2009

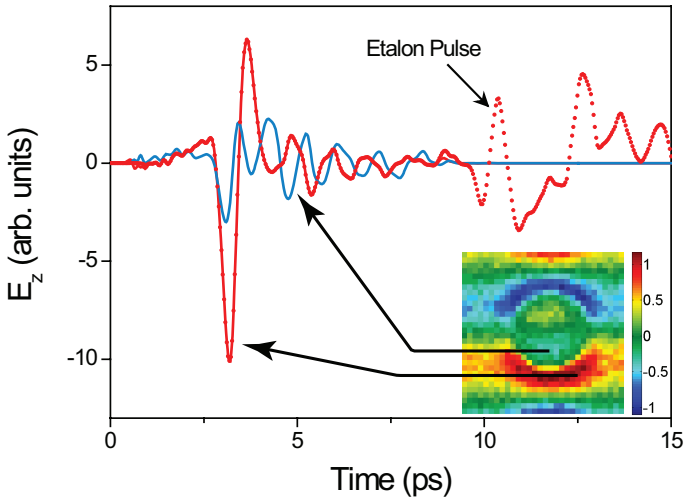

(a) Time-domain data for two pixels, one at the aperture edge (red) and the other within the aperture (blue). (Media 1)Inset shows an image of E_z at a time of 3.81 ps; $E_{Incident}$ is linearly polarized in the sample plane, vertical relative to the image. Data are windowed before the first etalon pulse. Raw data from the aperture edge are displayed as a dotted red line; the solid red line shows the same data after windowing.

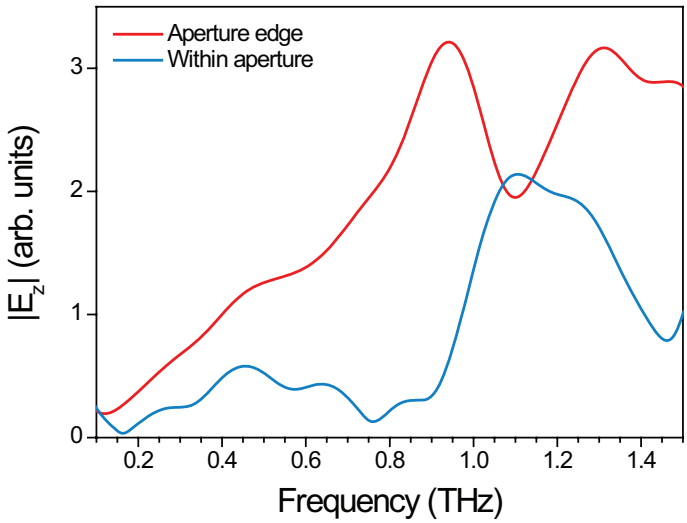

(b) $|E_z|$, normalized to the incident THz field. The red (blue) curve corresponds to spectral information for the red (blue) time-domain pulse in (a).

Fig. 8. Time- and frequency-domain data for E_z from a single aperture in the middle of the P = 90 μm array.

#113121 - $15.00 USD Received 19 Jun 2009; revised 7 Aug 2009; accepted 7 Aug 2009; published 11 Aug 2009

with the incoming light, then the field we observe within the aperture might be explained as a manifestation of Wood's anomaly [37]. This phenomena occurs in diffraction gratings, when the diffracted light is tangent to the plane of the grating, thus resulting in a minimum at a given diffraction order. For a grating with square lattice and light at normal incidence, the frequency at which we should expect to observe a minimum from Woods anomaly is given by [38]:

$$\lambda = \frac{a_o}{\sqrt{m^2+n^2}}\sqrt{\varepsilon_d} \tag{1}$$

where m,n corresponds to the diffraction order, a_o = array period, and ε_d is the real part of the substrate dielectric constant. For the P = 90 μm array on a GaP substrate ($\varepsilon_{GaP} = 10.89$), this corresponds to a frequency of 1.01 THz for the $(0,\pm1)$ and $(\pm1,0)$ diffraction orders. This is close to the minimum we observe in the spectrum at the aperture edge, as well as the concomitant maximum we observe within the aperture. The minimum at the aperture edge might originate from interference between the light emerging from the aperture and diffracted light which is propagating parallel to the array surface. Similar effects are observed for a different array with larger apertures and a different periodicity (d = 200 μm, P = 300 μm; data not shown here). Preliminary numerical simulations also show the presence of a longitudinal component underneath the apertures. However, more work must be done in order to clarify its physical origin. This is currently under investigation.

4.2. Resonant contributions

The peaks observed in the E_z spectrum from the aperture edges of the P = 90 μm array (see Fig. 8) can also be explained as enhanced electromagnetic transmission, which is a consequence of resonant coupling of the THz light to surface plasmon polaritons (SPP) modes [16, 17, 40]. At normal incidence, and for an array with square lattice, the wavelength at which one should expect to observe resonant surface modes can be approximated by [3]:

$$\lambda = \frac{a_o}{\sqrt{m^2+n^2}}\left(\frac{\varepsilon_m\varepsilon_d}{\varepsilon_m+\varepsilon_d}\right)^{\frac{1}{2}} \approx \frac{a_o}{\sqrt{m^2+n^2}}\sqrt{\varepsilon_d} \tag{2}$$

where a_o is the array periodicity, m and n are integers, ε_d is the real part of the dielectric function for the dielectric interface and ε_m is the real part of the dielectric function for the metal. At THz frequencies, the dielectric function of typical metals becomes quite large and they behave like perfect electric conductors. Note that this is not a limitation for the formation of bound surface modes, so long as the surface is structured [12, 39, 40]. In the limit of large ε_m, the approximate wavelength of surface plasmon resonances is then given by the right-hand side of Eq. 2. In the P = 90 μm array spectrum (see Fig. 7 and Fig. 8), Eq. 2 predicts peaks in the transmission at 1.01 THz, corresponding to the mode (m,n) = $(\pm1,0)$, and at 1.42 THz, corresponding to the next higher-order mode (±1, ±1). These values are very close to the peaks we observe at 0.96 THz and a broad peak at $\sim$ 1.42 THz in the measured spectrum. In subsequent references to SPP modes, we will not differentiate positive versus negative (m,n) in the notation.

Signatures of resonant array contributions are also manifested in the spectra of the x-component and y-field components. In Fig. 9 we plot the transmission of the x-component of the field, normalized to the incident field, for a single pixel from an aperture in the middle of the P = 160 μm array. The sample was measured in a nitrogen-purged environment. Peaks in the transmission spectrum, indicated with arrows, match well with SPP contributions predicted by Eq. 2 ($\varepsilon_d = \varepsilon_{GaP} = 10.89$). Note that not all of the higher-order modes are well resolved. In particular, we only observe a slight shoulder near 1.13 THz where we should observe the (2,0) mode. One must, however, bear in mind that the spectrum shown in Fig. 9 is not the integrated spectrum for the entire array; it is from a single pixel only, comprising an area that

#113121 - $15.00 USD Received 19 Jun 2009; revised 7 Aug 2009; accepted 7 Aug 2009; published 11 Aug 2009

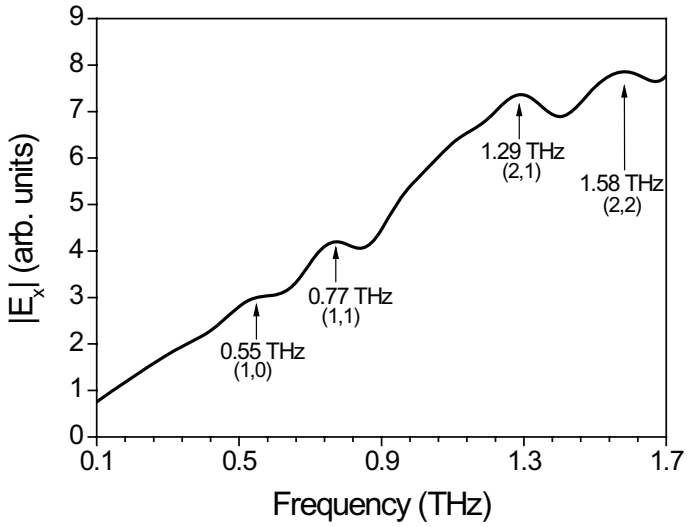

Fig. 9. E_X spectrum from a single pixel within an aperture in the middle of P = 160 μm array. Data were recorded in a nitrogen-purged environment. Arrows indicate peaks in transmission corresponding to predicted SPP modes.

is much smaller than the surface area of the whole aperture. One might therefore expect that, on a pixel-by-pixel basis, the weaker modes may be less well resolved. This might also help to explain why we do not observe a more significant transmission enhancement at resonant frequencies. Also recall that we measure the THz field within the GaP substrate. The coupling of THz light to surface modes as it emerges from and is diffracted by the apertures on this side of the array may be less efficient, relative to the air/metal interface. The large index mismatch between air and GaP is expected to reduce transmission enhancement for evanescent waves that are coupled on either side of the array [4]. The fact that the fundamental and next higher-order modes are not stronger can also be explained by this confluence of circumstances, along with the fact that these modes occur at frequencies that are below the cutoff frequency ($\nu_c = 0.89$ THz) for a circular waveguide with diameter, d = 60 μm. Recall that these apertures behave as if they are waveguides that are filled with their dielectric substrate. In spite of this, we are still able to resolve several resonant modes.

Though we observe signatures of SPPs in the transmission spectra of the arrays, we do not directly observe their presence in the time-dependent array images. A movie showing time-evolution of E_z as the field emerges from a single aperture in the middle of the P = 90 μm array is available online. In principle, this should be possible since we directly measure the longitudinal component of the THz near-field. In the time domain, one might expect to observe, for instance, a small field propagating away from the apertures in the direction of the incident THz polarization. The fact that we do not conclusively observe such a thing might be because the plasmon field is relatively weak when compared to the field at the aperture edges, which effectively eclipses everything around it. Even if we observe some THz light that seems to propagate along the surface, we could not necessarily differentiate between a propagating SPP and diffracted THz light grazing the surface. This is because, for small THz wavevectors, the dispersion curve of the SPP is not very different from the diffracted light line. In order to verify the presence of SPPs, one would need to measure the complete dispersion curve, which would require a much larger spatial measurement (e.g. farther away from aperture or edge). Another possibility is that SPPs might not be present. There are alternative explanations for

#113121 - $15.00 USD Received 19 Jun 2009; revised 7 Aug 2009; accepted 7 Aug 2009; published 11 Aug 2009

extraordinary optical transmission that rely on other mechanisms exclusive of, or in addition to SPPs, though we will not explore them in detail here [41, 42].

Near-field images of array subsections at resonant frequencies can provide additional insight into the potential role of plasmons or other resonant processes in shaping interactions among the apertures. For instance, a very interesting phenomena can be observed in the x-component of the field for both arrays at a frequency close to the first SPP mode (at the metal/GaP interface: 1.01 THz for the P = 90 μm array, and 0.568 THz for the P = 160 μm array). In Fig. 10, we show amplitude and relative phase images of E_x for the P = 160 μm array at 0.579 THz. Bright color

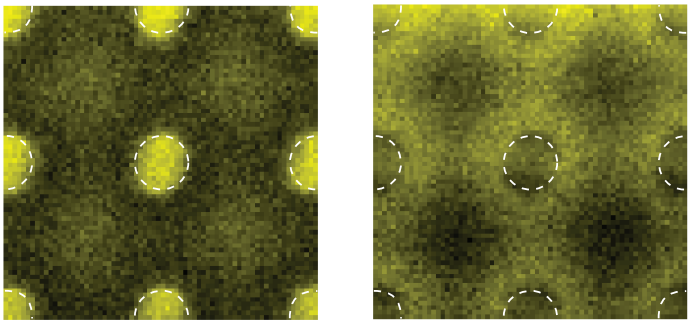

(a) E_x amplitude image (b) Relative phase image for E_x

Fig. 10. Amplitude and phase images for the P = 160 μm array at 0.579 THz. Scan area: 350 μm x 350 μm. White lines indicate approximate aperture positions.

corresponds to high field amplitude and dark color to low field amplitude. This frequency is very close to the first resonant surface wave contribution at 0.568 THz on the metal/GaP interface (the (1,0) mode). Note the presence of field in the spaces between the rows and columns of apertures. The relative phase of these features is similar to the phase of the field emerging from the apertures. This effect is much more prominent and easy to see for the larger array shown in Fig. 10, but also seems to be present in the P = 90 μm array (not shown). This is likely due to the smaller spacing between the apertures in the smaller array. One might think that since this field appears at resonant SPP frequencies, it could be a result of constructive SPP interference. We do not directly image plasmons when measuring the transverse field components very close to the array. If there is interference between plasmons, then the only way to observe this would be if, somehow, the resultant field is scattered into forward propagating electromagnetic radiation. However, since our measurement technique integrates the field for a small distance in the electro-optic detection crystal, especially in the case of the propagating field component, E_x, it might be possible to observe an x-component originating from plasmons or plasmon interference. One must also consider the fact that the fields appear in the spaces between the aperture rows. The plasmons that are coupled to the array should mirror the incident THz polarization, making it seem less likely that the plasmons would somehow interfere and form an x-component at these locations. It seems far more likely that such interference would be located directly above and between the apertures. If these effects are not coming from SPPs, then perhaps they originate from interference of diffracted light due to the presence of the array. Further studies are needed to confirm this.

5. Conclusion

Measurements of the x-, y-, and z-components of the THz electric near-field as they emerge from subwavelength apertures and aperture arrays illustrate how light interacts with these

#113121 - $15.00 USD Received 19 Jun 2009; revised 7 Aug 2009; accepted 7 Aug 2009; published 11 Aug 2009

structures and can also reveal how they interact with each other. This is information that can be difficult to obtain in a far-field measurement, where such interactions may be inferred rather than directly measured. In this work, we have shown not only how THz light emerges from single subwavelength apertures, but also how both resonant and diffractive processes are manifested in the near-field and may contribute to the overall spectrum of aperture arrays. An understanding of near-field interactions, such as the behavior of evanescent light and surface plasmons will be essential for potential future applications in near-field microscopy and spectroscopy, amongst other applications.

Acknowledgements

We gratefully acknowledge financial support from the Nederlandse Organisatie voor Wetenschappelijk Onderzoek (NWO) and from the EU TERANOVA Program (RCN-71835). This work was also supported by the Korea Science and Engineering Foundation (KOSEF) grant funded by the Korea government (MEST). Sandia is a multiprogram laboratory operated by Sandia Corporation, a Lockheed Martin Company, for the United States Department of Energy's National Nuclear Security Administration under contract DE-AC04-94AL85000.

#113121 - $15.00 USD Received 19 Jun 2009; revised 7 Aug 2009; accepted 7 Aug 2009; published 11 Aug 2009